Nonlinear elastic-plastic analysis of reinforced concrete column-steel beam connection by RBF-FD method

Pengfei Jiang[1], Hui Zheng[1*], Jingang Xiong[1], Pihua Wen[1,2]

1, *School of Civil Engineering and Architecture, Nanchang University, 330031, China*

2, *School of Engineering and Materials Science, Queen Mary University of London, UK*

Abstract: In this paper, the elastic-plastic analysis of cantilever beam and the Reinforced Concrete (RC) column-Steel (S) beam connection are studied using the Radial Basis Function- Finite Difference (RBF-FD) method. A direct method using bilinear nodes is proposed to deal with the instability caused by the first derivative calculation in the traditional RBF-FD method. Based on the idea of gradient projection method, the improved RBF-FD method is further applied to the multi-domain material nonlinearity. Numerical results are validated with the finite element method software (COMSOL).

Keywords: Radial basis function; Reinforced concrete column-steel beam; Finite element method; Collocation method

1. Introduction

The elastic-plastic deformation behavior in the most engineering solids is described by the Prandtl-Reuss increment theory and the Hencky-Ilyushin strain theory. The Finite Element Method (FEM) with increment theory for elastic-plastic problems is developed by Owen and Hinton [1]. The FEM is the most popular numerical method applied in engineering and science; however mesh generation may limit its application in large deformation problems. Meshless approximations based on interpolation techniques have received extensive attention since the diffusion element method proposed by Nayroles et al [2] and the radial basis function based on Euclidean distance has been applied to high dimensional problems successfully [3]. Currently, various types of numerical approaches with RBFs have been developed for different engineering problems [4-12]. The RBF-FD method is one of most famous numerical methods [6,13-16] with only need a few nodes to form a sparse matrix, which enhance the computational speed significantly. However, its derivatives cause instability [17-19]. In order to overcome this difficulty, the direct method, indirect method and fictitious node method are proposed [20-22]. The improved RBF-FD method has been successfully applied to different problems with phononic crystals. However, as the effective

*Corresponding author.

E-mail address: zhenghui@ncu.edu.cn

shear modulus in the RBF-FD method has to be continuous in the domain, the simulation of the multi-domain elastic-plastic Mechanics by the RBF-FD method can hardly be found [23].

The Reinforced Concrete column-Steel (RCS) beam frame structures are multi-domain structures that have been widely used in high-rise buildings at low earthquake risk areas since 1986 [24]. The joint area of the RCS composite structure locates at the cross section of a reinforced concrete column and structural steel [25]. The mechanical properties in the joint area keep the same values under certain loads, and there is no slip between the concrete slab and the steel beam. In order to analysis the joint area of the RCS composite structure, the FEM software such as ANSYS, COMSOL and ABAQUS are often applied to simulate the RCS structure [26-28]. The corresponding results can be validated by analyzing the mechanical response and the deformation in connection [29-32]. The FEM is the most popular method for the RCS composite structure simulation, and few works based on other numerical methods can be found [33-37].

In this work, the RBF-FD method is extended to the elastic-plastic analysis of the RCS joint. The projection method proposed by Desikan and Sethuraman [38] is introduced to deal with the nonlinearity based on the Hencky's deformation theory [39], and the effective shear modulus technique in [23] is applied. The numerical model of the elastic-plastic analysis with a cantilever beam and the RCS joint is established. The stability and accuracy of the RBF-FD method for elastic-plastic problems are validated with the results given by the FEM. The structure of this work is presented as following. In section 2, the RBF-FD method with elastic-plastic iteration is described in details. The numerical accuracy and stability are discussed in section 3. In section 4, numerical results of a quasi-static compression analysis of RCS connection are carried out. The conclusions and future works are given in section 5.

2. The RBF-FD method for elastic-plastic problems

In this section, the elastic-plastic theory and the projection method by considering equivalent shear modulus are briefly introduced.

2.1 Introduction of elastic-plastic theory

Considering elastostatics, the elastic equilibrium equations are given by

$$\sigma_{ij,j} + f_i = 0, \tag{1}$$

where f_i and $\sigma_{ij,j}$ denote the physical force vector and stress tensor respectively. The relationship between strain and displacement is

$$\varepsilon_{ij} = \frac{1}{2}\left(u_{i,j} + u_{j,i}\right). \tag{2}$$

The solid strain in the elastic-plastic state can be presented as the sum of the elastic and plastic strains

$$\varepsilon_{ij} = \varepsilon_{ij}^{e} + \varepsilon_{ij}^{p}, \tag{3}$$

where ε_{ij}^{e} and ε_{ij}^{p} are parts of elastic strain and plastic strain, respectively. The relationship between strain and stress can be given as

$$\varepsilon_{ij}^{e} = \frac{1+\nu}{E}\sigma_{ij} - \frac{\nu}{E}\delta_{ij}\sigma_{kk}, \tag{4}$$

where δ_{ij} is the Kronecker tensor symbol, E elasticity modulus, ν Poisson ratio. According to Hencky's theory [38], the plastic strain can be expressed as

$$\varepsilon_{ij}^{p} = \frac{\psi}{2G}\sigma'_{ij}, \tag{5}$$

where deviatoric stress tensor σ'_{ij} can be expressed as

$$\sigma'_{ij} = \sigma_{ij} - \delta_{ij}\sigma_{m}, \tag{6}$$

where σ_m is the hidrostatic stress, and ψ is a scalar valued function given as

$$\psi = 3G\frac{\bar{\varepsilon}^{p}}{\bar{\sigma}}, \tag{7}$$

$\bar{\varepsilon}^{p}$ and $\bar{\sigma}$ are equivalent plastic strain and equivalent stress,

$$\bar{\varepsilon}^{p} = \sqrt{\frac{2}{3}\varepsilon_{ij}^{p}\varepsilon_{ij}^{p}}, \tag{8}$$

$$\bar{\sigma} = \sqrt{\frac{3}{2}\sigma'_{ij}\sigma'_{ij}}. \tag{9}$$

Substituting Eqs. (4) to (9) into Eq. (3) produces

$$\varepsilon_{ij} = \left(\frac{1+\nu}{E} + \frac{\psi}{2G}\right)\sigma_{ij} - \left(\frac{\nu}{E} + \frac{\psi}{6G}\right)\delta_{ij}\sigma_{kk}. \tag{10}$$

Comparing Eqs. (4) and (10), the difference between plastic and elastic states in terms of the equivalent coefficient gives

$$\frac{1}{E_{eff}} = \frac{1}{E} + \frac{\psi}{3G}, \tag{11}$$

$$\nu_{eff} = E_{eff}\left(\frac{\nu}{E} + \frac{\psi}{6G}\right), \tag{12}$$

where E_{eff} and ν_{eff} denotes the equivalent Young's modulus and Poisson ratio. When the model is considered as the linear hardening material, the equivalent shear modulus in [23] is given as

$$G_{eff} = \frac{1}{3\bar{\varepsilon}}\left(\sigma_s + \frac{3E_T G\bar{\varepsilon}}{E} - \frac{\sigma_s E_T}{E}\right), \tag{13}$$

$$\Psi = \frac{G}{G_{eff}} - 1, \tag{14}$$

where E_T is tangent modulus beyond the yield stress σ_s, and G is shear modulus. The equivalent strain is defined as

$$\bar{\varepsilon} = \sqrt{\frac{2}{3}\varepsilon_{ij}\varepsilon_{ij}}. \tag{15}$$

According to the equivalent coefficient conversion model derived above, the 2D stress-strain relationship can be expressed as

$$\sigma_{11} = D_{11}\varepsilon_{11} + D_{12}\varepsilon_{22}, \sigma_{22} = D_{21}\varepsilon_{11} + D_{22}\varepsilon_{22}, \sigma_{12} = \sigma_{21} = S\varepsilon_{12} = S\varepsilon_{21}, \tag{16}$$

where subscripts 1 and 2 denote x_1 and x_2, respectively, and the material properties of the elastic model are given as

$$D_{11}(x_1, x_2) = D_{22}(x_1, x_2) = \frac{E}{(1-\nu^2)}, \tag{17}$$

$$D_{12}(x_1, x_2) = D_{21}(x_1, x_2) = \frac{E\nu}{(1-\nu^2)}, \tag{18}$$

$$S(x_1, x_2) = \frac{E}{2(1+\nu)}, \tag{19}$$

the effective coefficient of plane-stress elastic-plastic are evaluated as

$$D_{11}(x_1, x_2) = D_{22}(x_1, x_2) = \frac{E_{eff}(1-\nu_{eff})}{(1+\nu_{eff})(1-2\nu_{eff})}, \tag{20}$$

$$D_{12}(x_1, x_2) = D_{21}(x_1, x_2) = \frac{E_{eff}\nu_{eff}}{(1+\nu_{eff})(1-2\nu_{eff})}, \tag{21}$$

$$S(x_1, x_2) = \frac{E_{eff}}{2(1+\nu_{eff})}. \tag{22}$$

By substituting Eq. (16) and (2) into equilibrium Eq. (1), 2D elastic-plastic equation can be obtained. The displacements are specified as

$$u_i(x_1, x_2) = \mathrm{g}(x_1, x_2), \tag{23}$$

on the displacement boundary Γ_u, and the tractions are

$$\sigma_{ij}\boldsymbol{n}_j = \bar{\boldsymbol{t}}_i, \tag{24}$$

on the traction boundary Γ_σ, where $\boldsymbol{n}_j$ denotes the outwards normal vector at the boundary node.

2.2 Gradient projection method

The calculation process of the project method for elastic-plastic problem is shown in Fig. 1, where the stress and strain are depicted by two axes. The computation procedure is given as below.

Step 1, the position of node A is determined firstly for certain loads on the boundary

with the elastic model.

Step 2, the equivalent coefficient can be obtained by Eqs. (11) and (12) with the stress and strain at node A. Then the location of node B in Fig. 1 can be found with the equivalent coefficient and the strain of node A.

Step 3, the position of node C is obtained by considering the same loads applied on the boundary with the elastic analysis.

Step 4, following the same rule in step 2, based on node C, the position of node D can be obtained.

Repeat the above process until the variation of the numerical results satisfy

$$\eta = \frac{1}{N}\sum_{i=1}^{N}\frac{\left|E_{eff}^{(n)} - E_{eff}^{(n-1)}\right|}{E} < \eta_0, \tag{25}$$

where N is the total number of nodes, and η_0 is the convergence tolerance.

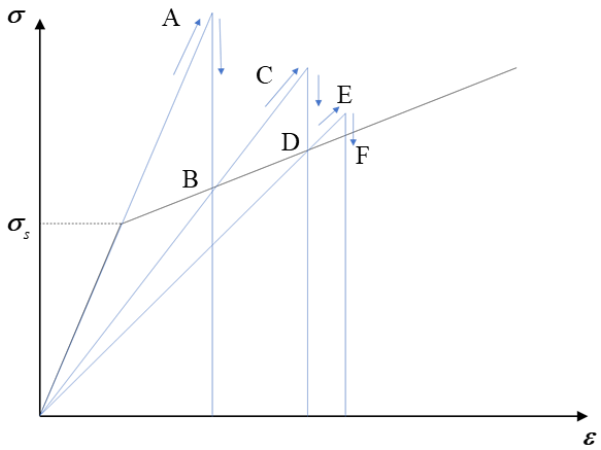

Fig. 1 The iterative process of equivalent modulus method for linear hardening material

2.3 2D multi-domain elastic-plastic

A 2D problem with multi-domains is considered as shown in Fig. 2. Substituting Eqs. (16) and (2) into Eq. (1) yields

$$\begin{cases} D_{11}u_{1,11} + Su_{1,22} + D_{11,1}u_{1,1} + S_{,2}u_{1,2} + \left(D_{12} + S\right)u_{2,12} + D_{12,1}u_{2,2} + S_{,2}u_{2,1} + f_1 = 0, \\ \left(D_{21} + S\right)u_{1,12} + D_{21,2}u_{1,1} + S_{,1}u_{1,2} + D_{22}u_{2,22} + Su_{2,11} + D_{22,2}u_{2,2} + S_{,1}u_{2,1} + f_2 = 0. \end{cases} \tag{26}$$

These coefficients of elastic-plastic D_{ij} and S are calculated by Eqs. (17)-(22). With the fixed boundary conditions on Γ_u given as

$$u_1\left(x_1, x_2\right) = 0,\ u_2\left(x_1, x_2\right) = 0, \qquad \left(x_1, x_2\right) \in \Gamma_u, \tag{27}$$

and free boundary conditions given as

$$\begin{cases} \sigma_{11}\left(x_1, x_2\right) n_1 + \sigma_{12}\left(x_1, x_2\right) n_2 = 0, \\ \sigma_{21}\left(x_1, x_2\right) n_1 + \sigma_{22}\left(x_1, x_2\right) n_2 = 0, \end{cases} \quad \left(x_1, x_2\right) \in \Gamma_\sigma, \tag{28}$$

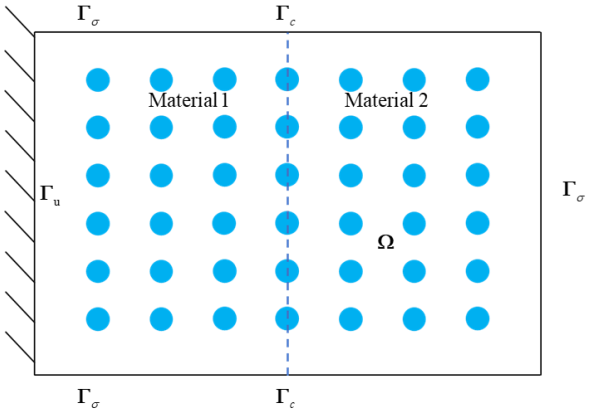

Fig. 2 A 2D elasto-plastic problem with two domains

The displacement continuity condition at the interface Γ_c can be given as

$$u_1^{(1)}\left(x_1, x_2\right) = u_1^{(2)}\left(x_1, x_2\right), \; u_2^{(1)}\left(x_1, x_2\right) = u_2^{(2)}\left(x_1, x_2\right), \; \left(x_1, x_2\right) \in \Gamma_c, \tag{29}$$

where $u_1^{(1)}, u_2^{(1)}$ and $u_1^{(2)}, u_2^{(2)}$ are the displacements at the interface of material 1 and material 2, respectively. The traction continuity condition at the interface Γ_c can be given as

$$\begin{cases} \sigma_{11}^{(1)}\left(x_1, x_2\right) n_1^{(1)} + \sigma_{12}^{(1)}\left(x_1, x_2\right) n_2^{(1)} = \sigma_{11}^{(2)}\left(x_1, x_2\right) n_1^{(2)} + \sigma_{12}^{(2)}\left(x_1, x_2\right) n_2^{(2)}, \\ \sigma_{21}^{(1)}\left(x_1, x_2\right) n_1^{(1)} + \sigma_{22}^{(1)}\left(x_1, x_2\right) n_2^{(1)} = \sigma_{21}^{(2)}\left(x_1, x_2\right) n_1^{(2)} + \sigma_{22}^{(2)}\left(x_1, x_2\right) n_2^{(2)}, \end{cases} \left(x_1, x_2\right) \in \Gamma_c. \tag{30}$$

2.4 The RBF-FD method descriptions

With RBF function $\tilde{u}(\boldsymbol{x})$ can be approximated as

$$\tilde{u}(\boldsymbol{x}) = \sum_{n=1}^{N_s} \phi\left(\left\|\boldsymbol{x} - \boldsymbol{x}_n\right\|\right) \alpha_n, \tag{31}$$

where N_s is the number of interpolating nodes in the local domain, as shown in Fig. 3. α_n are unknown coefficients to be solved, ϕ is the RBF. In this work, the Multi-quadratic is employed

$$\phi\left(r_n\right) = \sqrt{r_n^2 + c^2}, \tag{32}$$

where $r_n = \left\|\boldsymbol{x} - \boldsymbol{x}_n\right\|$ denotes the Euclidean distance and c is the shape parameter. In the uniform nodes distribution, the shape parameter is related to the node distance [40-41]. In this work, the shape parameter is selected by using test functions method given in [42]. Several test functions are used for the same problem, and the optimal shape parameter c can be

simply determined with the error observation. More details of the shape parameters can be found in [42-44]. Elastic-plastic analysis is carried out with uniformly distributing nodes as shown in Fig. 3.

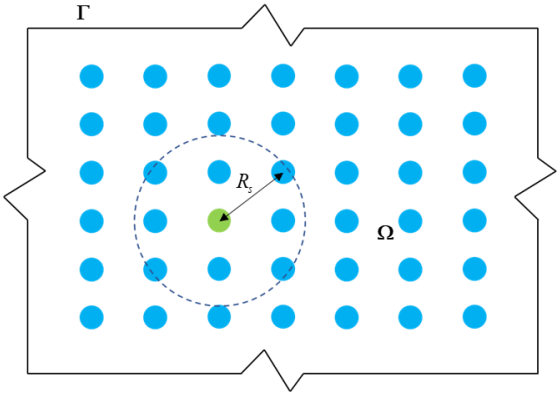

Fig. 3 The local interpolation range at a node in the RBF-FD method

From Eq. (31), by using the neighboring nodes for each source node, we have

$$\boldsymbol{\alpha}_n = \bar{\boldsymbol{\Phi}}^{-1}\bar{\boldsymbol{u}}, \tag{33}$$

where $\bar{\boldsymbol{\Phi}} = \left[\phi\left(\left\|\boldsymbol{x}_j - \boldsymbol{x}_l\right\|\right)\right]_{1\le l,j\le N_s}$ is the RBF interpolation matrix with size of $N_s \times N_s$, and $\bar{\boldsymbol{u}} = \left[u(\boldsymbol{x}_1),\ldots,u(\boldsymbol{x}_{N_s})\right]^T$ is the vector of displacement with size of $1\times N_s$. Letting

$$\Theta = \left[\phi\left(\left\|\boldsymbol{x} - \boldsymbol{x}_1\right\|\right),\ldots,\phi\left(\left\|\boldsymbol{x} - \boldsymbol{x}_{N_s}\right\|\right)\right], \tag{34}$$

and substituting Eq. (33) and (34) into Eq. (31), the solution and its differential form can be expressed as

$$\tilde{u}(\boldsymbol{x}) = \sum_{n=1}^{N_s}\phi\left(\left\|\boldsymbol{x}-\boldsymbol{x}_n\right\|\right)\alpha_n = \Theta\bar{\boldsymbol{\Phi}}^{-1}\bar{\boldsymbol{u}}, \tag{35}$$

$$L\tilde{u}(\boldsymbol{x}) = \sum_{n=1}^{N_s}L\phi\left(\left\|\boldsymbol{x}-\boldsymbol{x}_n\right\|\right)\alpha_n = L\Theta\bar{\boldsymbol{\Phi}}^{-1}\bar{\boldsymbol{u}}. \tag{36}$$

For simplicity we define

$$\boldsymbol{\Phi} = \sum_{n=1}^{N_s}\phi\left(\left\|\boldsymbol{x} - \boldsymbol{x}_n\right\|\right)\bar{\boldsymbol{\Phi}}^{-1} = \Theta\bar{\boldsymbol{\Phi}}^{-1}, \tag{37}$$

$$L\boldsymbol{\Phi} = \sum_{n=1}^{N_s}L\phi\left(\left\|\boldsymbol{x} - \boldsymbol{x}_n\right\|\right)\bar{\boldsymbol{\Phi}}^{-1} = L\Theta\bar{\boldsymbol{\Phi}}^{-1}, \tag{38}$$

where the size of $\boldsymbol{\Phi}$ and $L\boldsymbol{\Phi}$ is $1\times N_s$, L is the differential operator. Then Eqs. (35) and (36) can be expressed as

$$\tilde{u}(\boldsymbol{x}) = \boldsymbol{\Phi}\bar{\boldsymbol{u}}, \tag{39}$$

$$L\tilde{u}(\boldsymbol{x}) = L\boldsymbol{\Phi}\bar{\boldsymbol{u}}. \tag{40}$$

By inserting zeros at proper position, the above equations can be further expressed as

$$\tilde{u}(\boldsymbol{x}) = \boldsymbol{\Phi}\bar{\boldsymbol{u}} \underset{\text{local}}{\overset{\text{global}}{\rightleftarrows}} \dot{\boldsymbol{\Phi}}\boldsymbol{u}, \tag{41}$$

$$L\tilde{u}(\boldsymbol{x}) = L\boldsymbol{\Phi}\bar{\boldsymbol{u}} \underset{\text{local}}{\overset{\text{global}}{\rightleftarrows}} L\dot{\boldsymbol{\Phi}}\boldsymbol{u}, \tag{42}$$

where $\boldsymbol{u}$ is the vector of the displacements at all nodes, the size of $\boldsymbol{u}$, $\dot{\boldsymbol{\Phi}}$ and $L\dot{\boldsymbol{\Phi}}$ is $1\times N$, where N is the number of all nodes. The discretization matrix can be formed by considering Eqs. (41) and (42) in Eqs. (26)-(30). The stress and strain can be obtained by Eqs. (16) and (2). The first derivative is evaluated by the direct method, where 3 bilinear local nodes are employed to calculate the first derivatives as shown in Fig. 4. The calculation of the normal derivative by considering bilinear nodes for 2D or 3D case is thus reduced to a 1D case in the one direction, the accuracy and stability of derivative calculation will be improved. More details please refer to [22].

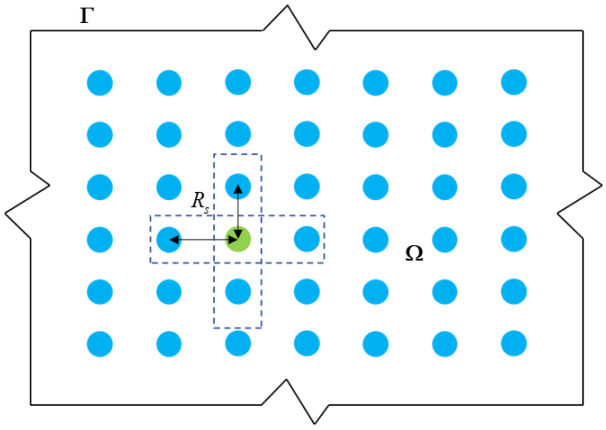

Fig. 4 The bilinear nodes in one direction

3. Discussion of stability

In this section, the numerical stability of the RBF-FD method is discussed by a cantilever beam. Furthermore, the details of the stress and strain obtained from the RBF-FD method and FEM are fully discussed.

3.1 Stability analysis

In this case, a 2D cantilever beam is subjected to a load $P=5\times10^{7}N$ at the end of right-hand side shown in Fig. 5. The length and width of the beam $L\times D=4m\times1m$, and the material properties are given as: Elasticity modulus $E=200GPa$, Poisson ratio $v=0.25$, yielding stress $\sigma_s=235MPa$. The tangent modulus after the yield stress is $E'=0.2E$. The uniformly distributed nodes with gap d are considered, and 9 local nodes are employed to

guarantee the shape of each local domain is a square. Unlike the traditional RBF-FD method, 3 bilinear nodes are used to evaluate the first derivative in the improved RBF-FD method. The shape parameters can be determined by the trial function proposed in [42].

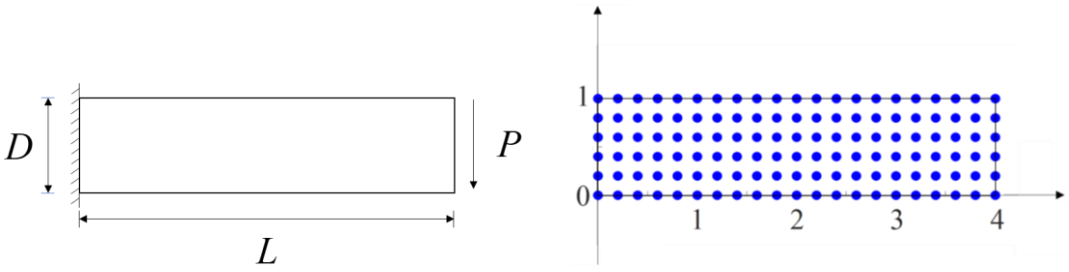

Fig. 5 Cantilever beam model (left) and node distribution (right, the gap d=0.2m)

In order to show the improvement of the improved RBF-FD method, the relative errors of u_2 versus the different shape parameter c by the improved RBF-FD method and traditional RBF-FD method are given the Fig. 6. The improved RBF-FD method employs three bilinear nodes. The definition of relative error is $\sum|\boldsymbol{u}_f-\boldsymbol{u}_l|/\sum|\boldsymbol{u}_f|$, where $\boldsymbol{u}_f$ and $\boldsymbol{u}_l$ denote the displacements obtained from the FEM and RBF-FD method, respectively.

Numerical results show that, the numerical results obtained by the improved RBF-FD method are very close to the FEM when c=40 to 80. The improved RBF-FD method show a better numerical error, this validates the improvement by using the bilinear nodes in the improved RBF-FD method.

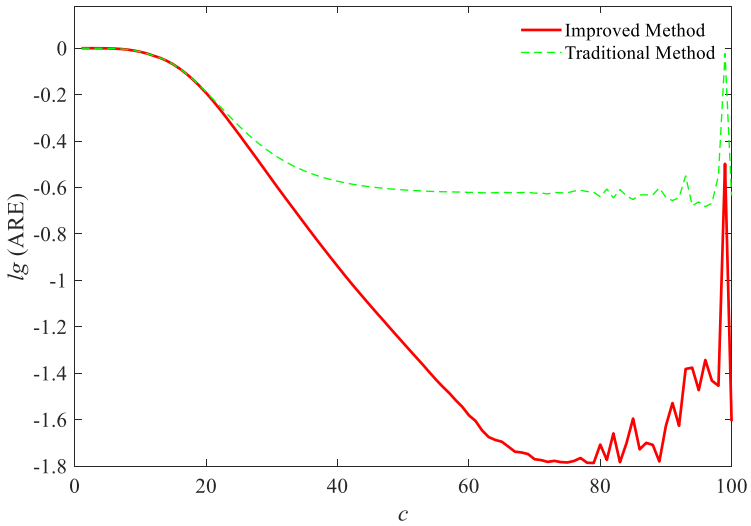

Fig. 6 The average relative errors of u_2 with different shape parameter c

The numerical results obtained by the improved RBF-FD method are further compared

and validated with the results by FEM (COMSOL). The uniform mesh generation used by FEM method is considered shown in Fig. 7. The grid size d of uniform distributed meshes can be used to control the number of meshes.

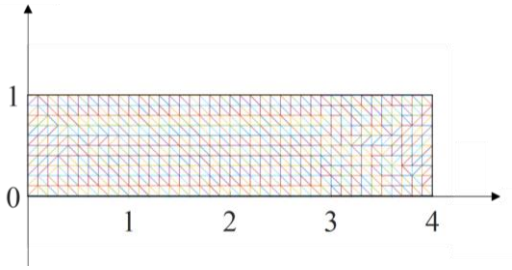

Fig. 7 The FEM uniform mesh with grid difference d

According to the numerical results, the results are stable after 10 iteration steps, and convergent solutions with the convergence tolerance $\eta_0 = 0.001$ in Eq. (25) can be obtained. The numerical results obtained from the RBF-FD method with $d=0.02m$ are close to the results by FEM as shown in Fig. 8. Excellent accuracy and convergence have been achieved.

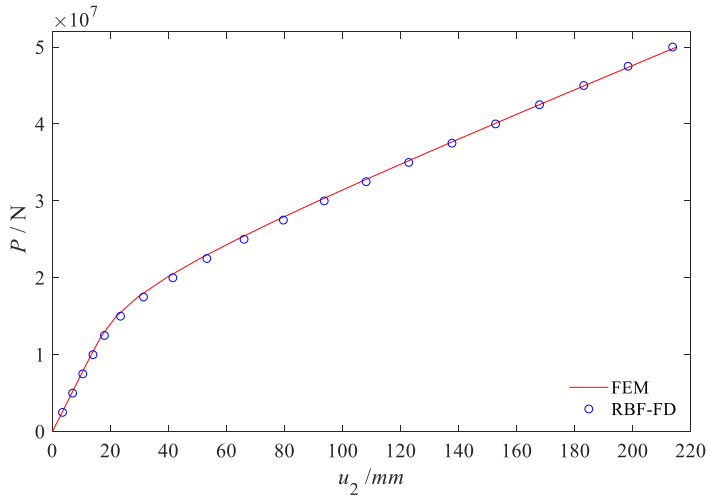

Fig. 8 The vertical displacement of (4,0.5) obtained by code under different loads

In addition, three different types of meshes are employed in the FEM, i.e. (a) uniform square grid with $d=0.1m$ as shown in Fig. 7, (b) triangular meshes as shown in Fig. 9, and (c) square mesh as shown in Fig. 7 with $d=0.05m$. The strains of the nodes located at Y= $1m$ are evaluated by the FEM and the RBF-FD method are compared in Fig. 10.

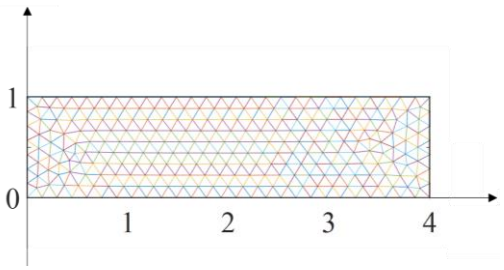

Fig. 9 The optimized mesh distribution

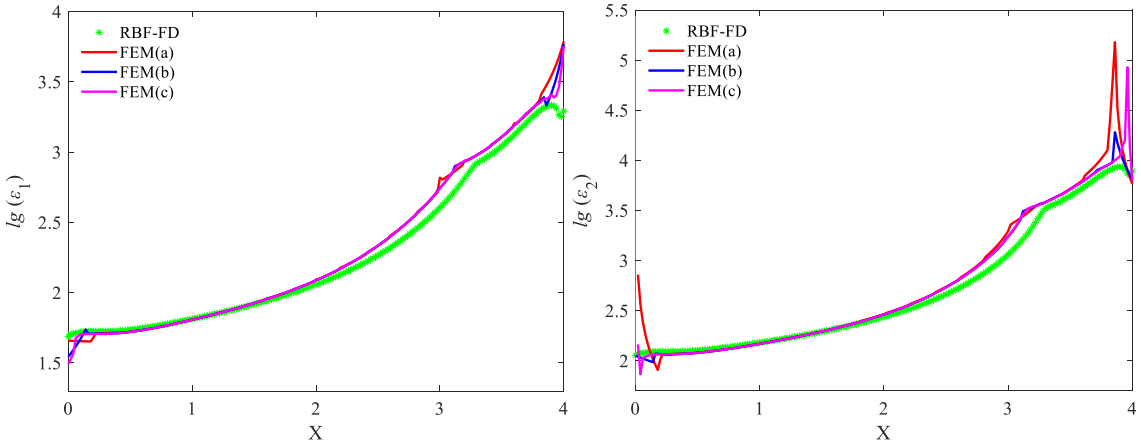

Fig. 10 The final strain in the axis X directions (left) and Y directions (right) at Y= 1m

The numerical results of the strain obtained by FEM and RBF-FD method in Fig. 10 have good agreement as well. However, largest difference can be observed near two fixed ends, where the stress distributions are singular. It can be found that the strain obtained by the RBF-FD method is smooth; however the results obtained from the FEM with different meshes show a large variant. This indicates the derivative calculation by using the FEM is not stable.

4. Numerical analysis of RCS joints

In this case, the RBF-FD method is applied to the beam-passed-through RCS connection. As shown in Fig. 11, a $4m\times0.4m$ steel beam penetrates through a concrete columns with two fixed ends, and the size of the two concrete columns is $0.4m\times0.5m$. A static uniformly distributed load $P=8\times10^7N$ is applied on the top of the column. The material constants of the steel beam are: Elasticity modulus $E=200GPa$, Poisson ratio $v=0.25$, yielding stress $\sigma_s=235MPa$. The tangent modulus after the yield stress is $E'=0.2E$. For the material constants of the concrete, the Elasticity modulus $E_c=25GPa$, Poisson ratio $v_c=0.2$. The results obtained from the FEM COMSOL software are used to compare and validate the numerical results of the RBF-FD method.

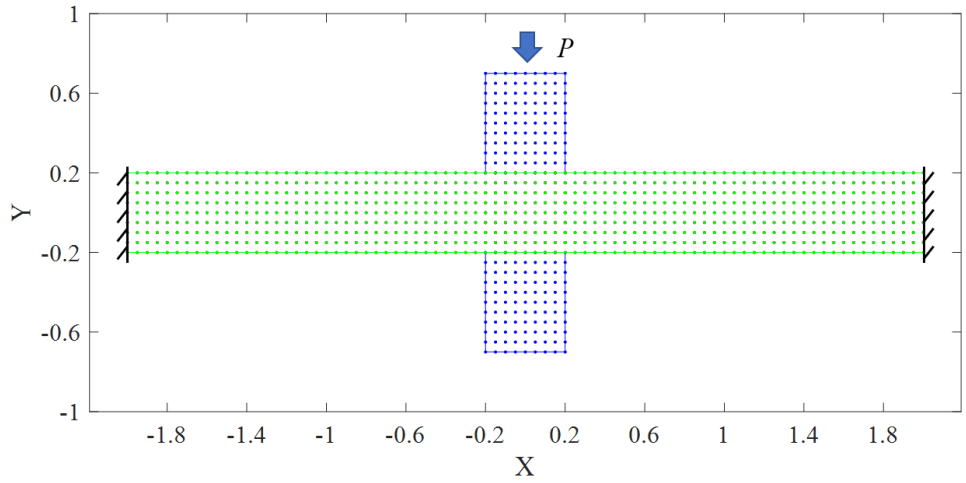

Fig. 11 The numerical model with grid difference d (greens are steel, blues are concrete)

The uniform nodes distribution with grid size $d=0.02m$ (the degree of freedom is 10702) is used in the RBF-FD method, the shape parameter $c=60$, 9 local nodes are considered. The continuity conditions in Eqs. (29) and (30) are considered at the interface. The triangular elements are implemented in FEM, the degree of freedom (DOFs) of the FEM is 101082.

The average relative errors with different iteration steps are given as Fig. 12. The average relative error is $\sum\left|\boldsymbol{u}_f-\boldsymbol{u}_l\right|/\sum\left|\boldsymbol{u}_f\right|$, where $\boldsymbol{u}_f$ and $\boldsymbol{u}_l$ denote the displacements obtained from the FEM and RBF-FD method, respectively.

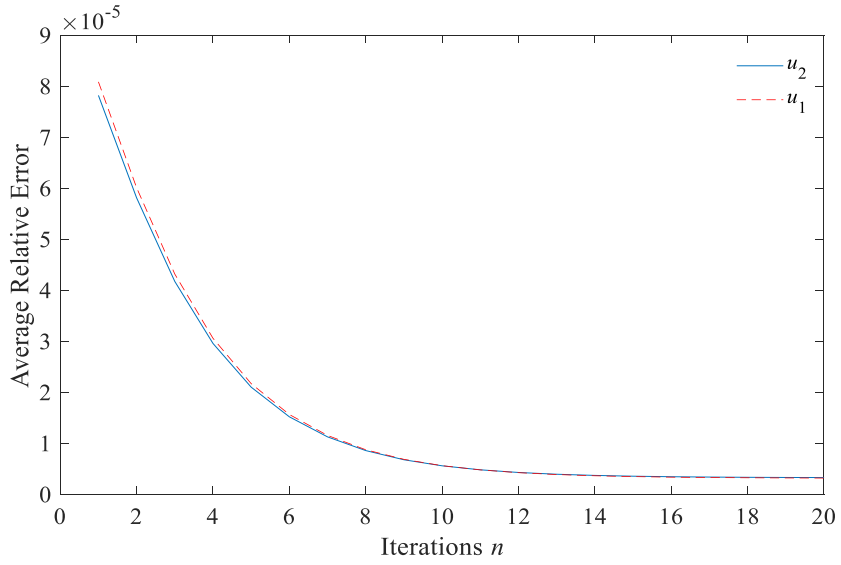

Fig. 12 The average relative error with the iterations

The convergence tolerance η is less than 0.001 after 14 iteration steps in this case.

However, 10 iteration steps are needed for the cantilever beam problem in example 1. In order to further study the RBF-FD method, the load displacements at node (0, -0.7) are given in Fig. 13. The numerical results obtained from the RBF-FD method and FEM show a high similarity.

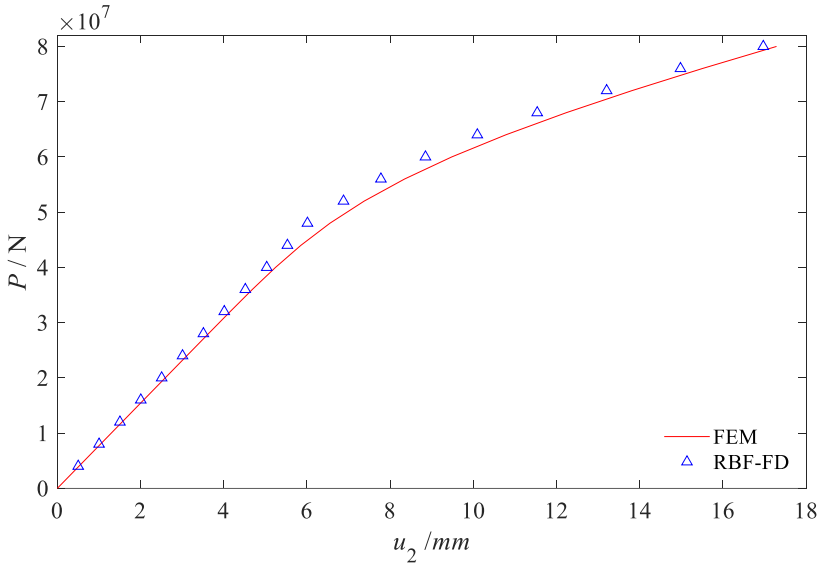

Fig. 13 The load-displacement curve at (0, -0.7)

As the structure of the numerical results is symmetric, we present the numerical results at the half part of the RCS joint. The stress of σ_{11} and σ_{12}, as well as the von Mises stress are presented in Fig. 14-Fig. 16 respectively.

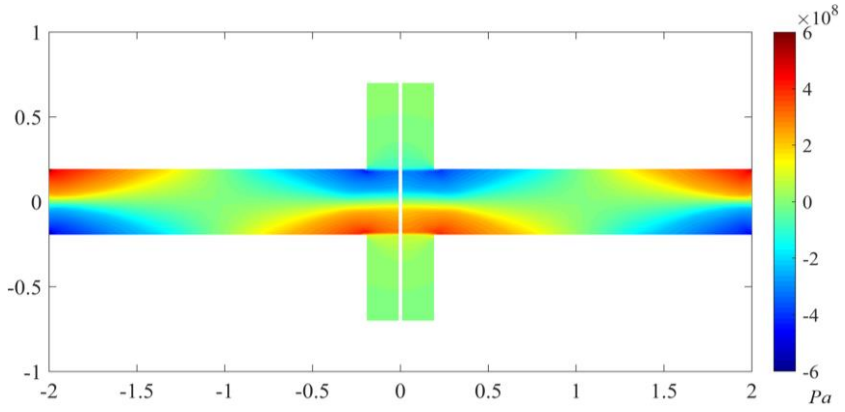

Fig. 14 Stress in the X direction obtained from RBF-FD method (left) and FEM (right)

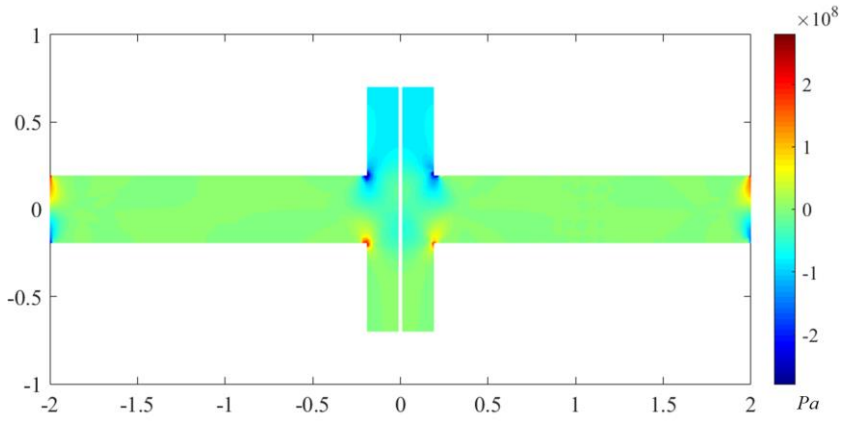

Fig. 15 Stress in the Y direction obtained from RBF-FD method (left) and FEM (right)

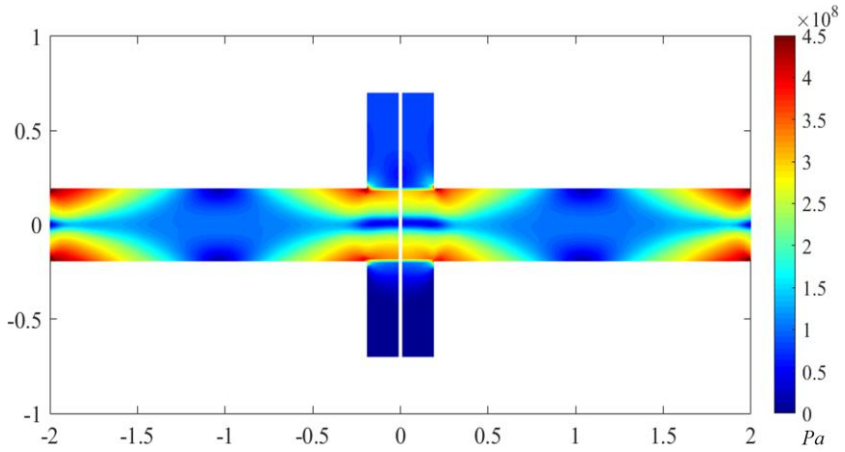

Fig. 16 Final von Mises stress obtained from RBF-FD method (left) and FEM (right)

The final deformation of the model after 10 times is presented in Fig. 17 to better show the numerical results.

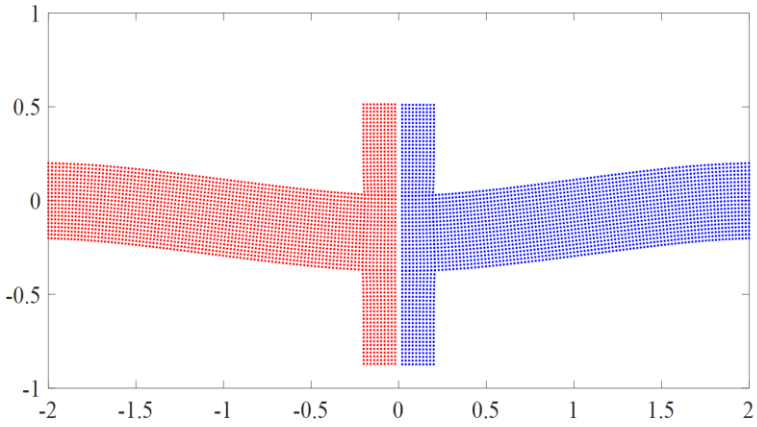

Fig. 17 Final deformation obtained from RBF-FD method (left) and FEM (right) /*mm*

The stress distributions of the beam-passed-through RCS show that, the stress concentrations can be observed at the corners between the concrete and steel. Therefore, certain engineering treatments will be carried out to reduce the damage in the local area. The numerical results of both FEM and RBF-FD method are of the same degree of accuracy in general. However, the stress and stain evaluated by the RBF-FD method will be smoother and more stable than that by the FEM.

5. Conclusion

The RBF-FD method is extended to the elastic-plastic calculation of the RCS joint in this paper. By applying the direct method, the stability of the RBF-FD method in solving the nonlinearity of the multi-domain elastic-plastic problem has been achieved. Numerical results show that the shape parameter in RBF-FD is not sensitive in computation of the improved RBF-FD method. The future work is to develop RBF-FD to 3D elastic-plastic problem in the RCS joint.

Acknowledgement

This work is acknowledged by National Natural Science Foundation of China (no: 11702125) and (no: 51768044) grant. The authors thanks to the Innovation Fund Designated for Graduate Students of Jiangxi Province (YC2020-B023) and the support of double thousand talents program from Jiangxi Provence.

Reference

[1] Owen D R J, Hinton E. Finite Elements in Plasticity: Theory and Practice. Pineridge Press, 1980.

[2] Nayroles B, Touzot G, Villon P. Generalizing the finite element method: Diffuse approximation and diffuse elements. Computational Mechanics, 1992, 10(5):307-318.

[3] Fasshauer G E, Zhang J G. On choosing "optimal" shape parameters for RBF approximation. Numerical Algorithms, 2007, 45(1-4): 345-368.

[4] Kansa E J. Multiquadrics—A scattered data approximation scheme with applications to computational fluid-dynamics—I surface approximations and partial derivative estimates. Computers & Mathematics with Applications, 1990, 19(8-9): 127-145.

[5] Kansa E J. Multiquadrics—A scattered data approximation scheme with applications to computational fluid-dynamics—II solutions to parabolic, hyperbolic and elliptic partial differential equations. Computers & Mathematics with Applications, 1990, 19(8-9): 147-161.

[6] Vertnik R, Sarler B. Meshless local radial basis function collocation method for convective‐diffusive solid‐liquid phase change problems. International Journal of Numerical Methods for Heat & Fluid Flow, 2006, 16(5): 617–640.

[7] Chi S W, Chen J S, Hu H Y. A weighted collocation on the strong form with mixed radial basis approximations for incompressible linear elasticity. Computational Mechanics, 2014, 53(2): 309-324.

[8] Mavric B, Sarler B. Application of the RBF collocation method to transient coupled thermoelasticity. International Journal of Numerical Methods for Heat & Fluid Flow, 2017, 27(5), 1064-1077.

[9] Martin B, Fornberg B. Using radial basis function-generated finite differences (RBF-FD) to solve heat transfer equilibrium problems in domains with interfaces. Engineering Analysis with Boundary Elements, 2017, 79: 38-48.

[10] Wang L H, Wang Z, Qian Z H, Gao Y K, Zhou Y T. Direct collocation method for identifying the initial conditions in the inverse wave problem using radial basis functions. Inverse Problems in Science & Engineering, 2018, 26(12): 1695-1727.

[11] Wang L H, Qian Z H, Zhou Y T, Peng Y B. A weighted meshfree collocation method for incompressible flows using radial basis functions. Journal of Computational Physics, 2019, 401: 1-18.

[12] Mishra P K, Fasshauer G E, Sen M K, Ling L. A stabilized radial basis-finite difference (RBF-FD) method with hybrid kernels. Computers & Mathematics with Applications, 2019, 77(9):2354-2368.

[13] Sarler B, Vertnik R. Meshfree explicit local radial basis function collocation method for diffusion problems. Computers and Mathematics with Applications, 2006, 51(8): 1269-1282.

[14] Hanoglu U, Sarler B. Multi-pass hot-rolling simulation using a meshless method. Computers & Structures, 2018, 194: 1-14.

[15] Hanoglu U, Sarler B. Hot rolling simulation system for steel based on advanced meshless solution. Metals, 2019, 9(7): 788.

[16] Mavric B, Dobravec T, Vertnik R, Sarler B. A meshless thermomechanical travelling-slice model of continuous casting of steel. IOP Conference Series Materials Science and Engineering, 2020, 861:012018.

[17] Hart E E, Cox S J, Djidjeli K, Kubytskyi V O. Solving an eigenvalue problem with a periodic domain using radial basis functions. Engineering Analysis with Boundary Elements, 2009, 33(2): 258-262.

[18] Hart E E, Cox S J, Djidjeli K. Compact RBF meshless methods for photonic crystal modelling. Journal of Computational Physics, 2011, 230(12): 4910-4921.

[19] Platte R B, Driscoll T A. Eigenvalue stability of radial basis function discretizations for time-dependent problems. Computers & Mathematics with Applications, 2006, 51(8): 1251-1268.

[20] Zheng H, Yang Z J, Zhang C Z, Tyrer M. A local radial basis function collocation method for band structure computation of phononic crystals with scatterers of arbitrary geometry. Applied Mathematical Modelling, 2018, 60:447-459.

[21] Zheng H, Zhang C Z, Wang Y S, Chen W, Sladek J, Sladek V. A local RBF collocation method for band structure computations of 2D solid/fluid and fluid/solid phononic crystals. International Journal for Numerical Methods in Engineering, 2017, 110(5): 467-500.

[22] Zheng H, Zhang C Z, Wang Y S, Sladek J, Sladek V. A meshfree local RBF collocation method for anti-plane transverse elastic wave propagation analysis in 2D phononic crystals. Journal of Computational Physics, 2015, 305:997-1014.

[23] Tu W, Gu Y T, Wen P H. Effective shear modulus approach for two dimensional solids and plate bending problems by meshless node collocation method. Engineering Analysis with Boundary Elements, 2012, 36(5): 675-684.

[24] Griffis L G. Some design considerations for composite-frames structures. Engineering Journal, AISC, 1986, 23(2): 59-64.

[25] Steele J P. Composite RCS frame systems: construction and performance. Texas A&M University, 2004.

[26] Azar B F, Ghaffarzadeh H, Talebian N. Seismic performance of composite RCS special moment frames[J]. KSCE Journal of Civil Engineering, 2013, 17(2): 450-457.

[27] Guo Z F, Men J J, Shi Q X, Tian J B. Research on Behavior of RCS Composite Joints. Advanced Materials Research, 2013, 671: 534-537.

[28] Ghods S, Kheyroddin A, Nazeryan M, Mirtaheri M. Nonlinear behavior of connections in RCS frames with bracing and steel plate shear wall. Steel and Composite Structures, 2016, 22(4): 915-935.

[29] Kanno R. Strength, deformation, and seismic resistance of joints between steel beams and reinforced concrete columns. Cornell University, 1993.

[30] Kanno R, Deierlein G G. Seismic behavior of composite (RCS) beam-column joint subassemblies. Proc., Compos. Constr. III, ASCE, 1997: 236-249.

[31] Cheng C T, Chen C C. Seismic behavior of steel beam and reinforced concrete column connections. Journal of Constructional Steel Research, 2005, 61(5): 587-606.

[32] Fargier-Gabaldón L B, Parra-Montesinos G J. Behavior of reinforced concrete column–steel beam roof level T-connections under displacement reversals. Journal of Structural Engineering, 2006, 132(7): 1041-1051.

[33] Sheikh T M, Deierlein G G, Yura J A, Jirsa J O. Beam-column moment connections for composite frames: Part 1. Journal of Structural Engineering, 1989, 115(11): 2858-2876.

[34] Deierlein G G, Sheikh T M, Yura J A, Jirsa J O. Beam-column moment connections for composite frames: Part 2. Journal of Structural Engineering, 1989, 115(11): 2877-2896.

[35] Parra-Montesinos G, Wight J K. Seismic response of exterior RC column-to-steel beam connections. Journal of Structural Engineering, 2000, 126(10): 1113-1121.

[36] Deierlein G G, Noguchi H. Research on RC/SRC column systems. 12th World Conference on Earthquake Engineering, 2000.

[37] Liang X, Parra-Montesinos G J. Seismic behavior of reinforced concrete column-steel beam subassemblies and frame systems. Journal of Structural Engineering, 2004, 130(2): 310-319.

[38] Desikan V, Sethuraman R. Analysis of material nonlinear problems using pseudo-elastic finite element method. J Pressure Vessel Technol, 2000, 122(4): 457-461.

[39] Ralph B. Basic engineering plasticity (an introduction with engineering and manufacturing applications). Materials Characterization, 2008, 59(3):348-348.

[40] Ferreira A J M, Fasshauer G E. Computation of static deformations and natural frequencies of shear deformable plates by an RBF-Pseudospectral method with an optimal shape parameter. Advances in Meshfree Techniques, 2007, 283-310.

[41] Schaback R. On the efficiency of interpolation by radial basis functions. Surface Fitting and Multiresolution Methods. 1997, 309-318.

[42] Zheng H, Yao G, Kuo L H, Li X. On the selection of a good shape parameter of the localized method of approximated particular solutions. Advances in Applied Mathematics and Mechanics, 2018, 10(4): 896-911.

[43] Issa K, Sanni B O. Smoothness for some selected test functions relative to shape parameter via IMQ. Mathematics and Decision Sciences, 2017, 17(2): 29-36.

[44] Liu C S, Liu D J. Optimal shape parameter in the MQ-RBF by minimizing an energy gap functional. Applied Mathematics Letters, 2018, 86: 157-165.